ADVANCED SUSTAINABLE SYSTEMS
www.advsustainsys.com

An Unexpected Source of Hard Carbon, Rice Hull Ash, Provides Unexpected Li^+ Storage Capacities

*Mengjie Yu, Man Wang, Sylvio Indris, Jason Manassa, Alex Stangel, Robert Hovden, and Richard M. Laine**

Hard carbon (HC) anodes used in secondary batteries have attracted increasing recent attention in particular to transition to new energy storage formats. To date, HC is produced exclusively by charring organic precursors in inert atmospheres. One would not expect to find HC in rice hull ash (RHA), the byproduct of rice hull combustion processes. However, in developing approaches to depolymerize RHA SiO_2 (90:10 wt% SiO_2:C) to produce silica-depleted RHA or $SDRHA_{40\text{-}60}$ (40–60 wt% SiO_2) to tailor C:SiO_2 ratios for carbothermal reduction reactions, the SDRHA carbon component is recently revisited. In more detailed efforts to characterize the form of carbon present in SDRHA, a series of analyses reveal graphitized carbon domains in amorphous matrices, i.e., HC, despite RHA being produced via combustion in an oxidizing atmosphere. Comprehensive electrochemical analyses on $SDRHA_{40\text{-}60}$ find unexpected capacities far in excess (>700 mAh g^{-1}) of reported values for HC and graphite. Electrochemical and STEM characterization suggest that the unexpected capacity may come from the nanoscale morphology of the amorphous carbon component. Given that RHA is a biowaste generated in kilotons/year worldwide, there seems to be an opportunity to develop sustainable high-capacity anode materials for alkali-ion storage systems.

1. Introduction

Decarbonization to mitigate global warming leading to environmental catastrophes requires urgent attention. To this end, one can envision three tiers of activity towards decarbonization. The first tier might be labeled decarbonization by direct CO_2 capture and stifling methane release. A second tier replaces fossil fuel use with sustainable energy generation, e.g., wind, solar, wave, coincident with energy storage techniques and electrification of power systems. The third tier involves replacing carbon and energy-intensive, large-scale industrial processes with less carbon-intensive or even carbon-neutral equivalents. The current work embraces tiers two and three by upcycling an agricultural waste, rice hull ash (RHA).

Biomass or agricultural waste-derived anode materials could be produced with net-negative CO_2 emissions and/or energy consumption,[1] superior to the notoriously large carbon footprint involved in the commercial production of graphite anodes that co-generates 5–10 tons of CO_2 per ton of battery-grade graphite.[2] In contrast, biomass combustion that transforms CO_2 captured via photosynthesis to combustible carbon is an overlooked source of green electrical energy. In particular, and in the US alone, rice hull combustion generates 100s of GW/year of electricity and coincidentally ≈150k tons/year RHA. Mostly treated as agricultural waste, RHA contains 80–90 wt% SiO_2, ≈10 wt% carbon and minor amounts of other inorganics and is frequently landfilled.

Previous efforts in this group developed multiple uses for RHA, including production of solar-grade (99.999%) silicon (Si_{pv}) and fumed SiO_2. Furthermore, via SiO_2 depolymerization reducing the SiO_2:C contents from 90 to 40 wt% or from 1.5:0.8 to 0.66:4 moles can provide low-cost materials, which by their nanocomposite nature greatly reduce reaction temperatures in the carbothermal production of Si_{pv}, silicon carbide (SiC), nitride (Si_3N_4), and oxynitride (Si_2N_2O).[3–5] We also demonstrated previously the utility of using silica-depleted RHA (SDRHA) derived SiC in Li^+ electrochemical devices but missed deeply assessing the carbon component other than as a reductant and typical byproduct of combusting biomass.[6–8]

Recent anode supplier source export restrictions and the increasing interest in alternative battery chemistries, e.g., sodium-ion batteries, have attracted investments towards securing more stable and lower-cost anodes, e.g., hard carbon (HC).[9–12] Indeed, most HC production should, in principle,

M. Yu, R. M. Laine
Macromolecular Science and Engineering
University of Michigan
Ann Arbor, MI 48109, USA
E-mail: talsdad@umich.edu
M. Wang, J. Manassa, A. Stangel, R. Hovden, R. M. Laine
Department of Materials Science and Engineering
University of Michigan
Ann Arbor, MI 48109-2136, USA
S. Indris
Institute for Applied Materials-Energy Storage Systems (IAM-ESS)
Karlsruhe Institute of Technology (KIT)
76344 Eggenstein-Leopoldshafen, Germany

The ORCID identification number(s) for the author(s) of this article can be found under https://doi.org/10.1002/adsu.202400667

DOI: 10.1002/adsu.202400667

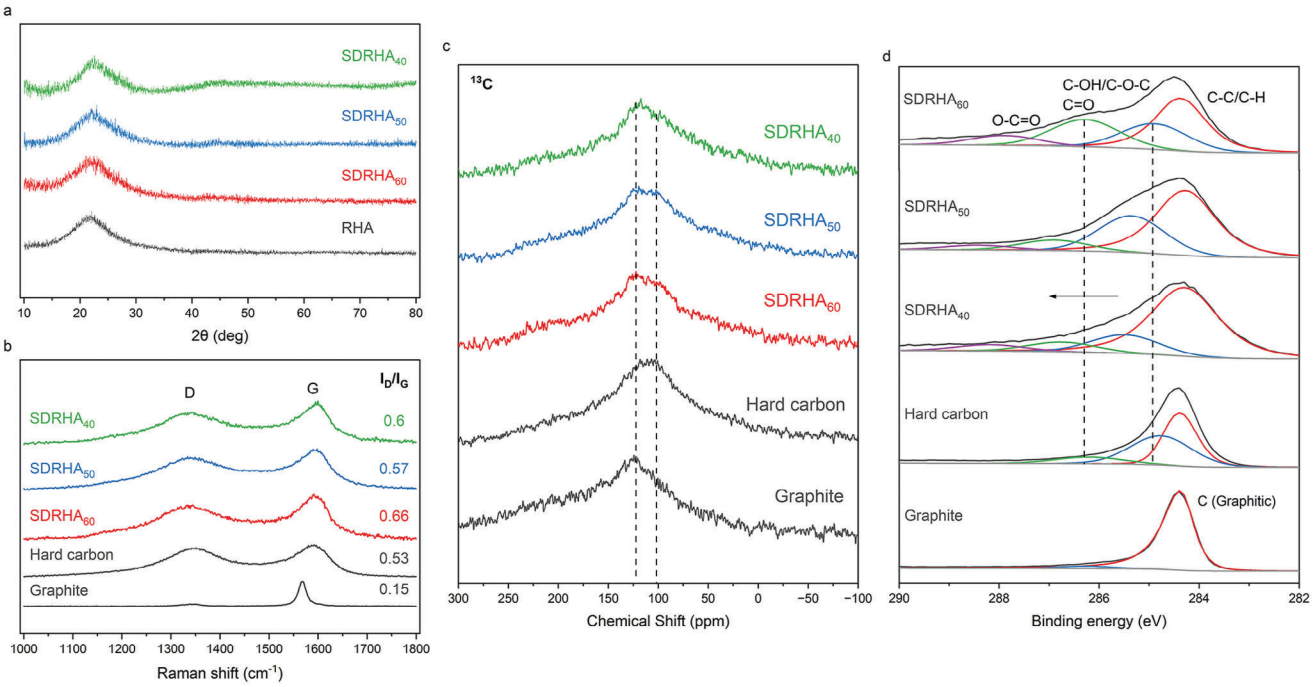

Figure 1. a) XRD, b) Raman spectra, c) ^{13}C NMR, and d) XPS C 1s of $SDRHA_{40\text{-}60}$. (y-axis corresponds to intensities with arbitrary units).

require less energy consumption than the >2000 °C graphitization reactions for synthetic graphite and extensive beneficiation treatments required to purify natural graphite thereby reducing byproduct CO_2 amounts.[13–15] As summarized in Table S1 (Supporting Information), most literature reports synthetic efforts to heat biomass to selectively produce HC use high temperatures and inert atmospheres.[16–18]

This contrasts greatly with rice hull combustion in air to produce RHA. RHA is easily purified by dilute acid followed by boiling water washing via ambient, low-energy processes.[3,4,19] Our approach builds on this using low-temperature SiO_2 depolymerization to generate spirosiloxane[20] that distills directly from the reaction solution leaving an easily recovered, high surface area HC with tunable performance in Li^+ devices through control of HC:SiO_2 ratios.

Inspired by increasing interest in low-cost, sustainable anode materials, we further characterized the carbon in SDRHA; and given our continuing interest in Li^+ energy storage systems, investigated its utility as a novel, green anode. Based on our previous work, we herein demonstrate the presence of domains of stacked graphene in an SDRHA porous carbon matrix by Raman spectroscopy and STEM, correlating SiO_2 depletion with SiO_2 structural and particle size changes in SDRHA. The electrochemical performance of SDRHA with various HC contents and the contribution of SiO_2 in the composites were further assessed to investigate the surprising and superior capacities obtained compared with literature values for HC and graphite as corroborated by coincidental comparison with anodes from commercial sources of these materials.

2. Results and Discussion

2.1. Hard Carbon in SDRHA

As discussed above, the carbon in SDRHA is produced coincidentally with RH combustion in an oxidizing environment. At this point, it seems likely that as combustion occurs, an SiO_2 layer forms encapsulating residual carbon preventing it from combusting. The encapsulated carbon is likely transformed during combustion to HC despite combustion residence times of just a few seconds to at most one minute.

Our earlier findings[4,6,7] per the profiles in **Figure 1a** suggest amorphous structures for both carbon and SiO_2 in RHA, as shown via broad XRD reflections at 23° 2θ. However, no effort was made to identify the formation of short-range ordered graphene regions in HC typically characterized by Raman, XPS, ^{13}C MAS NMR and TEM.[11,17] We herewith present such efforts followed by an assessment of Li^+ storage behavior.

2.1.1. Raman Spectra

Figure 1b presents the 1000–1800 cm^{-1} region for $SDRHA_{40,50\,60}$, a commercial hard carbon (C—HC), and a commercial graphite (C-G) revealing two major peaks: the G- and D-bands. The G-band at ≈1580 cm^{-1} is associated with the in-plane bending motion of sp^2 carbons, typical of graphitic carbon.[21,22] The G-band is sharp in graphite given its high degree of crystallinity. In comparison, this band broadens in the HC and $SDRHA_{40,50,60}$ samples, indicating increased disorder. The disorder-induced D-band

Table 1. SDRHA specific surface areas and Raman D:G ratios.

Material	BET SSA [m^2 g^{-1}]	I_D/I_G
$SDRHA_{40}$	510 ± 10	0.66
$SDRHA_{50}$	423 ± 38	0.57
$SDRHA_{60}$	345 ± 21	0.6
RHA	71 ± 13	-
C—HC	5	0.53
C-G	6	0.15

at ≈1340 cm^{-1}, arises from a ring breathing mode for doubly bonded carbon. In principle, the D-band first increases with disorder, then decreases and overlaps with other bands until it nearly disappears in highly amorphous carbon samples.[21,22]

The ratio of D- to G-band intensities (I_D/I_G) is a common parameter used to estimate the level of structural order. A low I_D/I_G value suggests a higher graphitization degree; a high I_D/I_G material has more disorder and structural defects.[22–24] Accordingly, the D- and G-bands were fitted to a Voigt shape, and the area under each peak was used to calculate I_D/I_G ratios due to the broadened nature of the band and width changes. As seen in **Table 1**, the I_D/I_G ratios of $SDRHA_{40,50,60}$ ($I_D/I_G \approx 0.6$) are higher than that of C—HC ($I_D/I_G \approx 0.5$). Nonetheless, the measured D-band and I_D/I_G ratios are close to the C—HC sample indicating ordered graphitic structures in $SDRHA_{40,50,60}$.

2.1.2. Solid-State NMR

Figure 1c ^{13}C NMR spectra of C-G exhibit one broad peak centered at ≈122 ppm, indicating high symmetry carbon packing.[25] In the C—HC and $SDRHA_{40,50,60}$ curves, the major signal is located at lower shift values (≈101 ppm), while a signal corresponding to graphene-like graphitic layers is also observed (≈124 ppm). This provides additional evidence concerning the carbon structural features in $SDRHA_{40,50,60}$ with short-range graphene stacking, where up-field shifted signals are associated with distortion between graphene layers.

2.1.3. XPS Analyses

Figure 1d compares peak fitting of carbon C 1 spectra for $SDRHA_{40,50,60}$ with C—HC and C-G. C 1s spectra for graphitic carbon are characterized by an asymmetric peak at a binding energy (BE) typically reported as 284.5 eV and a characteristic π–π^* shake-up structure centered at ≈291 eV.[26] In contrast, HC and $SDRHA_{40\text{-}60}$ C 1s spectra show broad and predominant C—C/C═C sp^2 peaks at 284.8 eV with additional C—H/C═C sp^3 peaks at 285–285.5 eV without asymmetry, as expected for disordered and defective carbon.[26,27] Peaks at 286–287, 287.5–288.5, and 288.5–290 eV are ascribed to C—O—C/C—OH, C═O, and O—C═O bonds, respectively.[28,29] The symmetric C—H/C═C sp^3 peaks of $SDRHA_{40,50,60}$ are broader and stronger than for C—HC, indicating more defect structures and C—O species. Meanwhile, the C—O peaks shift towards higher BEs with higher carbon contents in SDRHA, suggesting stronger C—O bonding in samples where more SiO_2 has been extracted ($SDRHA_{40}$).

2.1.4. BET Analyses

More oxygenated carbon surfaces are not unexpected given the much higher BET specific surface areas (SSAs) per the **Figure 2**a N_2 adsorption–desorption isotherm plots. As shown in Table 1, SSAs increase from ≈70 m^2 g^{-1} for RHA to ≈345 m^2 g^{-1} for $SDRHA_{60}$, while those for $SDRHA_{50,40}$ are ≈420, and ≈510 m^2 g^{-1}. N_2 adsorption–desorption isotherms correspond to type IV with H3 hysteresis per IUPAC classification, arising from a porous network in non-rigid aggregates of plate-like particles.[30]

In addition, Figure 2b pore size distributions indicate average pore size peaks centered at ≈4 nm for RHA. Additional peaks at <3 nm are seen in $SDRHA_{40,50,60}$, accompanied by relative mesopore volume increases with reduced SiO_2 contents.

2.1.5. STEM Imaging

Two morphologies are commonly observed in $SDRHA_{60}$, as seen in Figure 2 carbon region images. The first HAADF image (Figure 2c) shows a porous carbon network region, while Figure 2d shows a HAADF image of a carbon nanoparticle that resembles hard carbon. The hard carbon morphology had an entirely amorphous diffraction pattern. EELS analysis on a region of the hard carbon nanoparticle demonstrates that the hard carbon nanoparticle contains silica nanoparticles agglomerated on its surface (Figure 2e). Porous regions of the hard carbon have EELS fine structure consistent with the HC structure—here, a clear π^* peak consistent with amorphous carbon but also an early rising σ^* peak found in graphite and/or diamond (Figure 2f).

Overall, the above characterization results suggest $SDRHA_{xx}$ contains more complex carbon morphologies than traditionally manufactured C—HC, but still analyzing as HC with disordered and symmetric graphitic carbon features. The fact that SDRHA is a nanocomposite of carbon and SiO_2 is expected to result in considerable material at interfaces between the two phases resulting in more evident C—O bonding.

2.2. SiO_2 in SDRHA

To further understand the carbon and SiO_2 structures in SDRHA, the SiO_2 was isolated by oxidizing the carbon in oxygen. Figure S1a (Supporting Information) SEM of isolated SiO_2 particles from pristine RHA reveals plate-like structures with average particle sizes (APSs) >5 µm. In contrast, $SDRHA_{60}$ derived SiO_2 presents agglomerates with APSs <2 µm. EDS allows one to conclude that the particles >10 µm in $SDRHA_{60}$ are associated with HC, which are absent after heating in O_2. Figure S1b (Supporting Information) illustrates the N_2 adsorption and desorption plots for RHA and SiO_2 in RHA, corresponding to BET surface areas of ≈60 and ≈40 m^2 g^{-1}, respectively. Thus, during SDRHA synthesis the reactant and solvent HG likely depolymerize larger SiO_2 particles preferentially or more likely decreases SiO_2 APSs relatively uniformly.

The ^{29}Si MAS NMR spectra for $SDRHA_{40,50,60}$ (Figure S1c, Supporting Information) exhibit broad peaks at −112 ppm and shoulders at −102 ppm. The resolved signals are assigned to silicon-oxygen tetrahedral units with four neighboring [SiO_4]

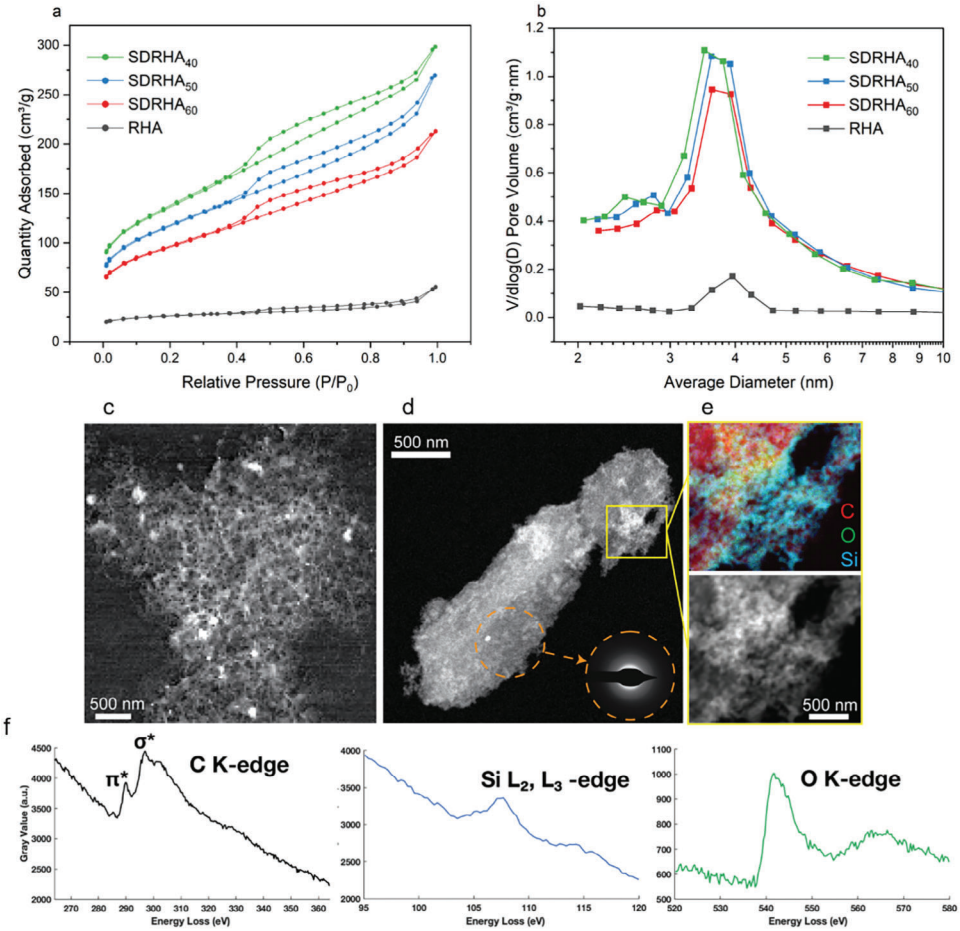

Figure 2. a) BET N_2 adsorption–desorption isotherm, b) pore-size distribution curves of $SDRHA_{40\text{-}60}$, HAADF STEM images of c) porous carbon network, d) carbon nanoparticle that resembles hard carbon with corresponding amorphous diffraction pattern, e) subregion of same carbon nanoparticle with simultaneously acquired EELS elemental composite, and f) Characteristic EELS spectra of C K-edge, Si L_2, L_3-edges, and O K-edge of $SDRHA_{60}$.

units, i.e., four so-called "bridging oxygen ions." The broad lines observed in the ^{29}Si NMR spectra are another indication of the amorphous SiO_2 framework with various [SiO_4] units and superpositions. These groups are consistent with Figure S1d (Supporting Information) XPS results where the O 1s spectra are fitted with O—Si—O bonding at ≈532.3 eV. Both samples show a small peak at ≈534 eV commonly assigned to coordinated —OH. The Si 2p region spectra were fitted with two peaks, one at ≈103 eV associated with Si—O_2 bonds and the other at a higher binding energy of ≈104 eV ascribed to silicon-oxygen tetrahedra with various numbers of siloxane (Si—O—Si) bonds.[31]

2.3. Electrochemical Analyses

Half cells with lithium metal as the counter electrode were assembled with $SDRHA_{40,50,60}$, RHA, and C—HC to compare their electrochemical performance in Li^+ systems. The CV curves at scan rates of 1, 3, 5, 7, 9, and 10 mV s^{-1} in 0.01–3 V are illustrated in **Figure** 3a,e,i and Figure S2a (Supporting Information). The CV curves are distorted from regular rectangles expected for ideal electrical double-layer capacitors (EDLCs). Meanwhile, the typical separated redox peaks in faradaic materials are not observed from the curves, suggesting pseudocapacitive behavior. As the scan rates increase, the CV charge/discharge corners shift upwards. This is presumably due to higher electrochemical polarization at high scan rates as ion adsorption/desorption onto electrode surfaces and breaking/forming of chemical bonds proceed at limited rates compared to the scan rate.[32] In this aspect, the material surface characteristics are important as they determine the reaction kinetic limits.

A widely adopted method to measure the capacitive effects in pseudocapacitive behavior has been defined by Dunn et al. via the following Equations:[33]

$$i\ (v) = i_{\text{capatitive}} + i_{\text{diffusion}} = av^b \quad (1)$$

$$i\ (V) = i_{\text{capatitive}} + i_{\text{diffusion}} = k_1\, v + k_2 v^{1/2} \quad (2)$$

where V is the potential, v is the sweep rate (mV s^{-1}).

In Equation (1), parameter b is determined from the slope of the linear plot of log i versus log v, as shown in Figure 3m from cathodic peaks at 1.5 V. In principle, if $b = 1$, the current response will be linearly proportional to the scan rate v, which

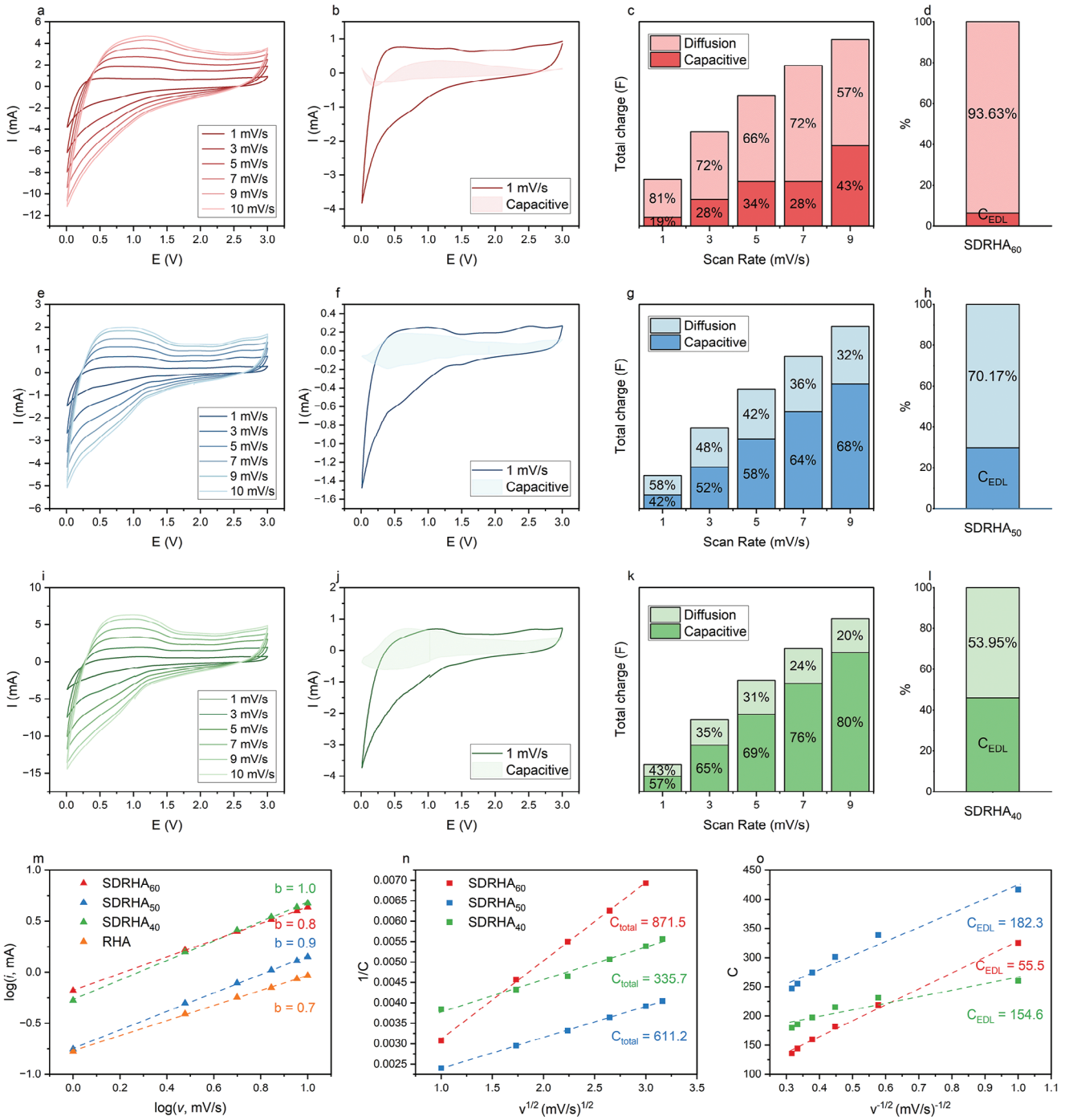

Figure 3. CV, Dunn method of capacitive contribution and Trasatti method for the contribution and EDL capacitance ratio of a–d) $SDRHA_{60}$/Li, e–h) $SDRHA_{50}$/Li, i–l) $SDRHA_{40}$/Li, m) Dunn method power law, and n,o) Trasatti method fittings.

signifies surface-controlled behavior in EDLC. In contrast, slow semi-infinite diffusion-controlled faradaic processes (battery type) exhibit $b = 0.5$.[34,35] Accordingly, the calculated slopes for RHA are $b = \approx 0.7$, while that for $SDRHA_{60}$, $SDRHA_{50}$ and $SDRHA_{40}$ are in the range of ≈0.8, ≈0.9, and ≈1, respectively, indicating that $SDRHA_{40,50,60}$ perform in a transition area from battery-like to capacitive-like responses, while surface reactions play a dominant role over diffusion-controlled reactions at the selected voltage.

In Equation (2), k_1 and k_2 are used to distinguish capacitive and diffusion currents, respectively, which can be evaluated from the slope and intercept of a linear plot of $i(V)/v^{1/2}$ versus $v^{1/2}$. This calculation quantifies the current contribution from the capacitive effects versus diffusion-controlled processes. Figure 3b,f,j

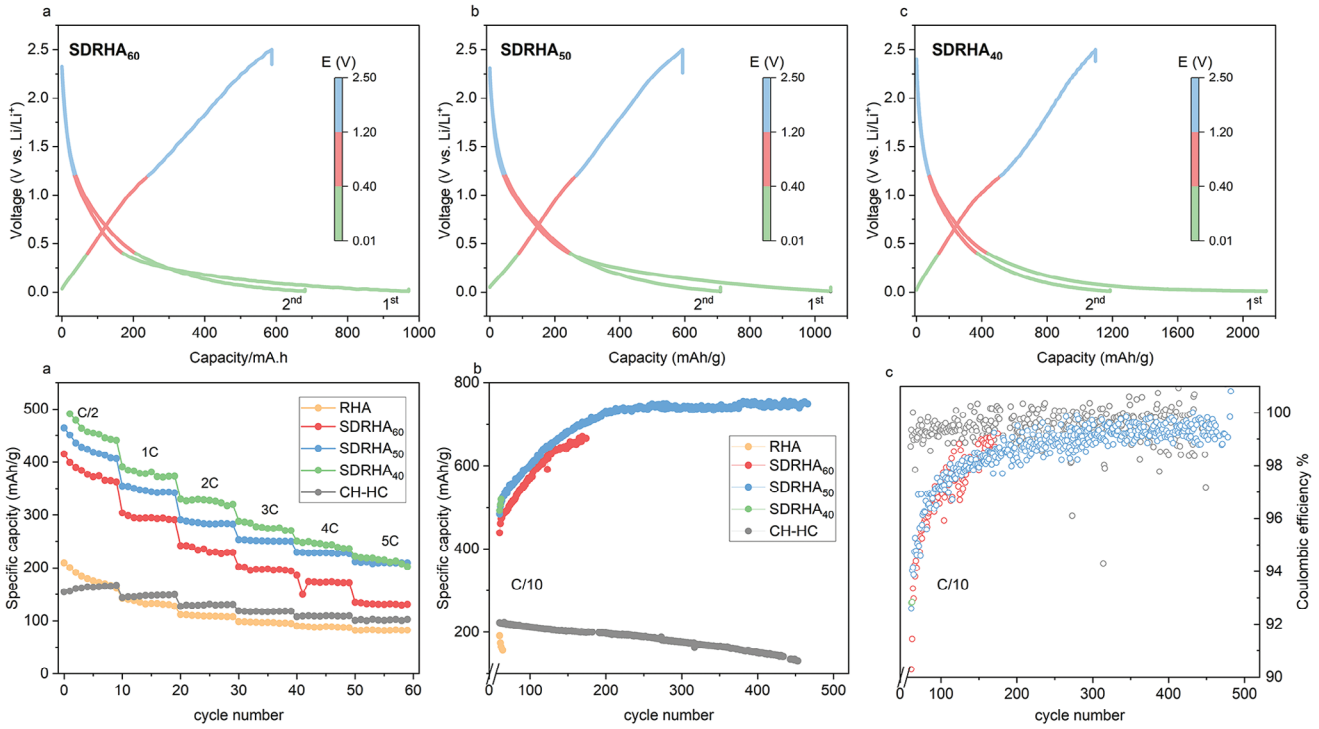

Figure 4. Voltage profiles for the 1st and 2nd cycles for a) $SDRHA_{60}$/Li, b) $SDRHA_{50}$/Li, c) $SDRHA_{40}$/Li. d) Rate capabilities, e) C/10 cycling and f) corresponding Coulombic efficiencies of $SDRHA_{40,50,60}$ compared to RHA and C—HC. Specific capacities normalized to the carbon components (1C = 300 mA g^{-1} are used for both SDRHA and C—HC). Only competed cycles averaged for three samples are recorded.

and Figure S2b (Supporting Information) provide examples of integrating 1 mV s^{-1} quantitative contributions from capacitive effects versus diffusion-controlled (battery-type) processes. Figure 3c,g,k and Figure S2c (Supporting Information) summarize these results at each scan rate, showing increased capacitive contributions at all scan rates with increases in HC:SiO_2 ratios, i.e., $SDRHA_{40}$ to $SDRHA_{60}$. The results suggest higher capacitive behavior is associated with high surface areas facilitating ion adsorption/desorption processes.

In principle, a large amount of charge is stored on both the outer and inner surfaces of the electrode at low scan rates due to more efficient time for ions to diffuse into the electrode surfaces. In contrast, at higher scan rates, most ions only access the outer electrode surface due to limited interaction times.

To assess the capacitive contribution from each process, the Trasatti method further differentiates pseudocapacitive and electrical double layer (EDL) processes. Assuming semi-infinite ion diffusion, the electrical double capacitance (C_{EDL}) and the total capacitance (C_T) can be obtained from the y-axis intercepts from the linear fitting of $C \sim \nu^{-1/2}$ (Figure 3n) and $C^{-1} \sim \nu^{1/2}$ (Figure 3o). As displayed in the bar charts for Figure 3d,h,l and Figure S2d (Supporting Information), the higher carbon contents and subsequently higher surface areas facilitate charge storage on the outer surfaces of the electrode, leading to higher contributions from EDL capacitance charge storage.

Figure 4a–c presents charge/discharge voltage profiles for the initial two cycles at C/10 between 0.01 and 2.5 V for $SDRHA_{40,50,60}$, where three major regions are observed. The initial sloping region >1.2 V, contributing ≈10% of the total capacities, arises from adsorption at surface defect sites and pore walls. The following region at 0.4–1.2 V is ascribed primarily to SEI formation during the first lithiation. The following slopes <0.4 V account for >50% of the total initial discharge capacity. It is widely accepted that Li^+ pore filling and intercalation into graphitic interlayers occurs in this region, whereas disordered-stacked carbon layers with higher interplanar spacing eliminate the staging transitions seen with graphite.[36] The above kinetic limitation discussion reveals diffusion-controlled processes at low rates. Therefore, the disordered nature and nanopores enable additional volume to be filled by Li^+ with time, providing additional capacity in $SDRHA_{60}$.

The following charge and discharge showed <10% of the capacities come from voltages >1 V while >85% capacities originate at <0.4 V. The irreversible Li^+ adsorption on surfaces results in low initial Coulombic efficiencies (CEs) in $SDRHA_{40,50,60}$, as seen in **Table 2**. Relatively low initial CEs are common characteristics and primary challenges for HCs used for Li^+ batteries. For instance, the initial discharge capacities and CE for C—HC are ≈320 mAh g^{-1}_{carbon} and ≈65%, respectively (Figure S3a, Supporting Information).

Electrochemical impedance spectroscopic (EIS) measurements were conducted after three cycles at C/10. Nyquist plot semicircles at <10 Hz are assigned to R_{SEI}, summarized in the inset table (Figure S3b, Supporting Information) The higher R_{SEI} in SDRHA suggests a thicker SEI forms than on C—HC, possibly arising from the higher SSAs and higher surface oxygenate contents (Figure 1d) which have been found to have significant effects on lithiation under some conditions.[37,38]

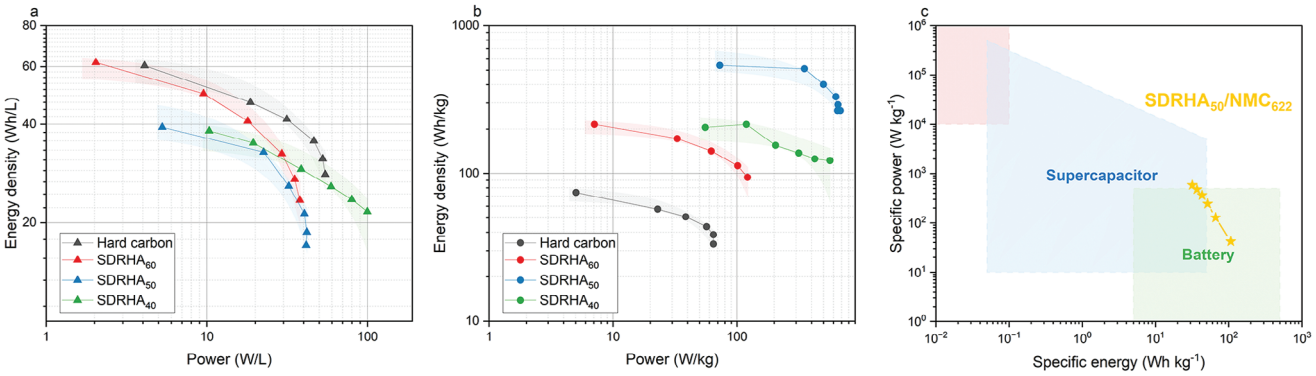

Figure 5. Ragone plots of a) volumetric and b) specific energy and power densities of $SDRHA_{40,50,60}$ normalized to the carbon components. c) $SDRHA_{50}/NMC_{622}$ performance comparison.

Table 2. Comparison of specific capacities of $SDRHA_{40,\ 50,\ 60}$ at different C rates.

Sample[a]	Initial	Specific capacity [mAh g^{-1}_{carbon}]						
		C/2	1C	2C	3C	4C	5C	C/10
$SDRHA_{60}$	585/970	360	290	225	190	170	130	640 (120 cycles)
$SDRHA_{50}$	593/1048	405	330	280	250	220	210	740 (420 cycles)
$SDRHA_{40}$	734/1317	425	340	280	240	220	200	530 (10 cycles)
RHA	560/268	170	130	110	95	86	80	150 (10 cycles)
C—HC	207/320	160	140	130	120	110	100	130 (400 cycles)

[a] Only carbon mass used to calculate specific capacities, ≈40 wt% of total electrode loading.

Figure 4d and Table 2 record rate capabilities for $SDRHA_{40,50,60}$and C—HC. Apparently, SDRHA shows more than double the discharge capacities of C—HC at C/2, 1C, 2C, 3C, 4C, 5C, resulting from the surface EDL capacitive contributions, as discussed above.

Figure 4e presents SDRHA cycling at C/10 following the rate capability tests, where unexpected capacity increments are observed. As recorded in Table S1 (Supporting Information), this phenomenon has been reported in other biomass-derived materials before, usually ascribed to "kinetic activation processes." For example, Campbell et al.[39] suggested doped K diffusion results in carbon lattice expansion, such that the micropores are more accessible to the electrolyte. In contrast to initial reactions that take place at the electrode surface, each subsequent oxidation/reduction occurs with more available pores and cavities, thereby increasing the specific capacity over time. Similar explanations were also reported in a study on N-doped carbon.[40] Other studies on oxides attributed the gradual increased capacity to the reversible growth of a polymeric gel-like film resulting from kinetically activated electrolyte degradation.[41–43]

The capacity increments observed in $SDRHA_{40,50,60}$ can be ascribed to HC with higher SSAs and smaller average pore sizes that facilitate capacitive processes where Li^+ absorbs on surfaces such as open pore walls. Continuous cycling drives Li^+ to slowly diffuse into inner areas via pore filling and intercalation between graphitic layers, thus exhibiting increasing Li^+ capacities. This is consistent with the above charge storage analyses (Figure 3).

Nonetheless, the diffusion-controlled release of Li^+ residing in the inner areas requires overcoming larger kinetic barriers.[44] As a result, the corresponding CEs (Figure 4f) start at ≈90% when the C rate was first reduced to C/10, then slowly improve to ≈99% when most inner areas were activated, i.e., reaching maximum capacities. Additionally, RHA shows capacity decays at all tested rates. The absence of capacity increments in RHA with lower SSAs and porosities (Figure 2) is another indication of the pore-induced capacity increases.

Meanwhile, as SDRHA is a SiO_2/HC nanocomposite, the increments are presumably related to both components. More detailed investigation in SiO_2 separated from SDRHA is discussed in the next section.

Ragone plots summarize the energy-power output properties of $SDRHA_{40,50,60}$ and C—HC in Li^+ half cells (**Figure 5**). In general, C—HC generally shows higher volumetric energy/power regions, while SDRHA samples exceed this performance when evaluated solely on the basis of carbon content as expected due to SDRHA's porous structures and, consequently, lower densities. Following our previous reported studies on $SDRHA_{65}$ (65 wt% SiO_2) with NMC_{622} as hybrid Li^+ supercapacitors,[6] when $SDRHA_{50}$ was tested with NMC_{622} cathodes, the corresponding outputs compared in Ragone plots suggest potential applications as high-power batteries.

2.3.1. SiO_2 in SDRHA

To understand the electrochemical behavior of SiO_2 versus HC in SDRHA, comparison studies were conducted by assessing the SiO_2 isolated from RHA and $SDRHA_{60}$ as discussed above. The voltage profiles between 0.01–2.5 V for the first two cycles at C/10 of SiO_2 are illustrated in Figure S6a (Supporting Information). The initial capacities are low at ≈32 mAh $g^{-1}_{RHA\text{-}SiO2}$ and ≈13 mAh $g^{-1}_{SDRHA60\text{-}SiO2}$, both showing low initial Coulombic efficiencies of ≈50% as reported in the literature.[45] It should be noted that the theoretical capacities for SiO_2, although controversial, are suggested to be 1950 mAh g^{-1}; thus, the current densities used for the SiO_2-based tests (1680 mAh g^{-1}) are higher than SDRHA (300 mAh g^{-1}). The low capacities for SiO_2 were also observed in other studies. Carroll et al.[46] ascribed these capacity discrepancies compared to other findings to the size and

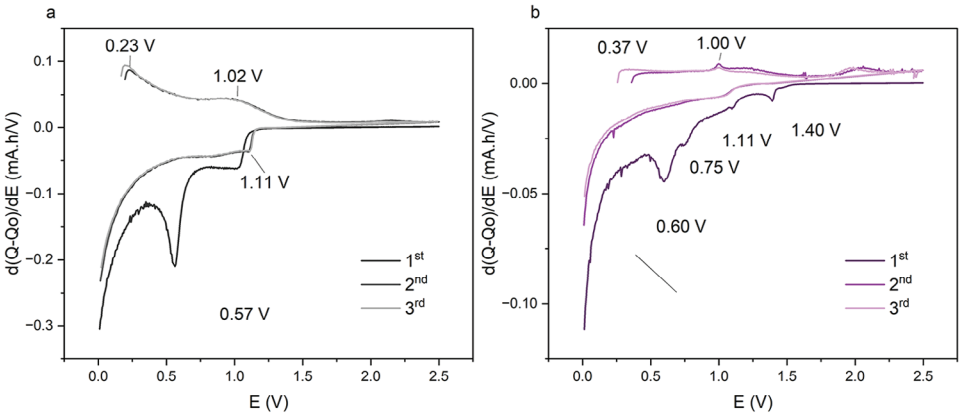

Figure 6. Differential capacity (dQ/dV) plots for the 1st and 2nd cycles for a) SiO_2 in RHA, and b) SiO_2 in $SDRHA_{60}$.

thickness of SiO_2, and the subsequent surface redox processes. Electrode properties also affect the measurements, while the purposes here are to compare SiO_2 with SDRHA thus the electrode parameters were remained the same.

The differential capacity–voltage plots (dQ/dV) for SiO_2 from RHA and $SDRHA_{60}$ (**Figure 6a,b**) are mostly identical. On initial lithiation, both types show a broad feature with an onset at 1 V that continues to 0.7 V. Commonly observed in SiO_2-based electrodes and other SiO_2 surface SEI, this redox peak is assigned to the formation of $Li_2Si_2O_5$.[46–48] The other observed peak at ≈0.56 V is ascribed to irreversible EC/DMC reduction.[49] This also suggests that a large proportion of capacities from the first cycle originate from SEI formation. Subsequent cycles show lithiation/delithiation peaks at ≈1 V, with no indication of Li_xSi (0.25 and 0.1 V for lithiation and 0.3 and 0.45 V for delithiation).

Coincidentally, there is an additional peak at ≈1.4 V for $SDRHA_{60}$-SiO_2 in the first lithiation, presumably related to irreversible lithium insertion in amorphous SiO_2.[50] Peaks at 2.05 V are shown in the 2nd and 3rd scans—delithiation at such a high potential is usually related to metallic redox suggesting lithium deposition on the Cu current collector, initiating oxidation of Cu^0 to Cu_2O and/or CuO.[51,52] Reasons for why deposition occurs for the SiO_2 from $SDRHA_{60}$ are not clear given the electrode preparation processes and parameters are identical for all samples. This remains a question for future studies.

These results are useful in understanding the behavior of SDRHA. Figure S4 (Supporting Information) compares differential capacity–voltage plots (dQ/dV) of $SDRHA_{50,60}$ with C—HC during the first two cycles at C/10 corresponding to Figure 4a–c. In $SDRHA_{50,60}$ peaks at 1–0.9 V and 0.8–0.7 V are likely overlaps of SEI formation on HC and irreversible SiO_2 reduction. Peaks at ≈0.5 V are likely associated with HC features in SDRHA, e.g., multi-scale porous structures. These peaks are absent during the following cycle, suggesting irreversible processes. Meanwhile, peaks at ≈0.23 V and ≈0.1 V still appear during the second cycle, where the former is consistent with the C—HC results (Figure S3, Supporting Information).

Dunn and Trasatti analyses for SiO_2 in RHA, and in $SDRHA_{60}$, are given in Figure S5 (Supporting Information). As expected, the smaller APSs for $SDRHA_{60}$-SiO_2 (Figure S1, Supporting Information) lead to higher capacitive current contributions. Thus, the increase in capacitive behavior from $SDRHA_{60}$ to $SDRHA_{40}$ is associated both with the high HC contents and smaller SiO_2 particles together facilitating ion diffusion kinetics. Meanwhile, the $SDRHA_{60}$-SiO_2 capacities remain flat during 500 cycles at C/10, while RHA-SiO_2 increases slightly by ≈2 mAh g^{-1}_{SiO2} after 400 cycles (Figure S6, Supporting Information). Apparently, the SiO_2 network structures in SDRHA after extraction differ from the original, which also impacts their electrochemical behavior with Li^+. Given that non-diffusion controlled processes dominate in $SDRHA_{60}$-SiO_2, as discussed above, the capacity increments in SDRHA should be associated mainly with the porous HC.

One may argue that, although rarely, SiO_x capacity increments are reported in the literature. Ban et al.[53] claimed to observe such effects in cycling $SiO_{1.83}$. The authors correlated experimental and simulation results to conclude that that the full reduction of SiO_2 is energetically unfavorable. Therefore, instead of forming Li_2O and Si—Si bonds by two Li atoms attacking an oxygen atom shared by SiO_4 tetrahedra, lithiation could proceed through partial reduction. When formed at the interface in SiO_γ ($\gamma < 2$), the volume fraction of Si increases, which can hold more Li. In some other cases, formation of Si/Li_xSi is reported on lithiated SiO_2, such as a report describing heating SiO_2/sugar mixtures to 1000 °C forming C/SiO_2 composites with immediate and stable capacities ≈600 mAh g^{-1} (10 cycles).[54] The following postmortem studies were undertaken to assess the likelihood of similar mechanisms operating in SDRHA.

2.4. Postmortem Studies

$SDRHA_{60}$ and C—HC half-cells, after 150 cycles, were de-crimped in an Ar-filled glovebox. **Figure 7a** C 1s core scans reveal peaks at 284.8, 285.2, and 287.1 eV that can be attributed to sp^2-hybridized C—C/C—H bonding, C—O, and C═O, respectively, in both cycled $SDRHA_{60}$ and C—HC electrodes. Meanwhile, C—HC electrodes show stronger peaks assigned to —CH_2— and —CF_2— species in PVDF,[55,56] and additional lithiated carbon C-Li compared to SDRHA electrodes.[57] It is widely accepted that SEI formation starts with Li—F and lithium alkyl carbonate polymerization.[58] With further growth, the organic components tend to decompose into more inorganic species including Li_2CO_3 and lithium fluorophosphates. This is observed in the C—HC with thinner SEI where more stable inorganic species concentrate near the

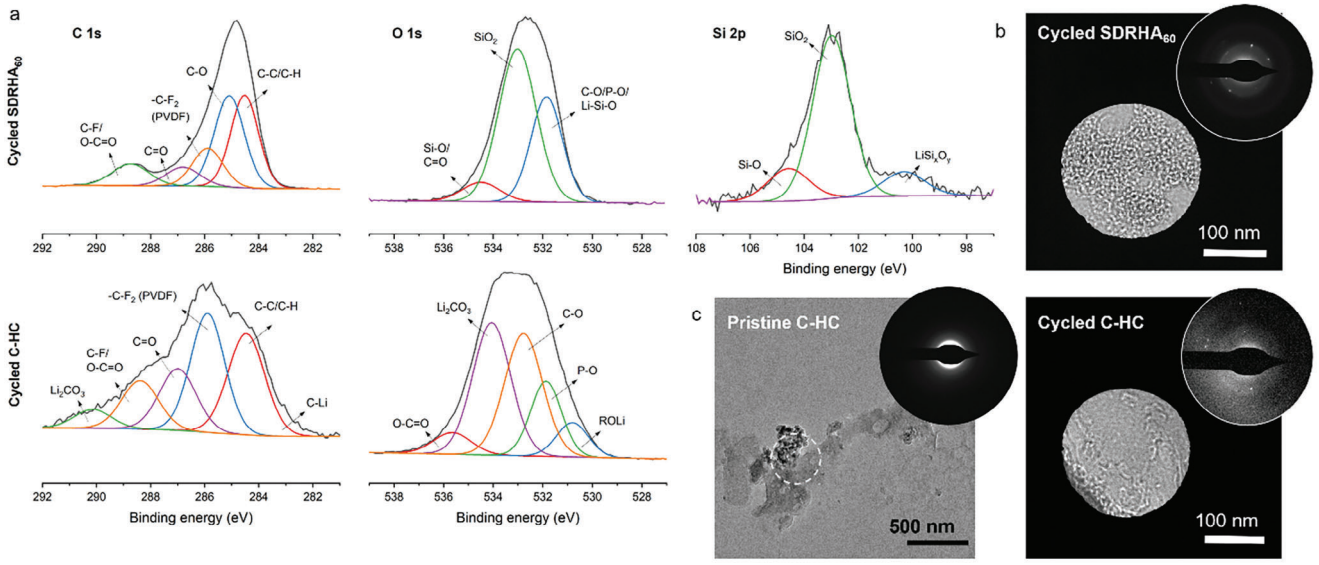

Figure 7. a) XPS C 1s, O 1s, and Si 2p core-level spectra of cycled $SDRHA_{60}$ and C—HC electrodes, STEM images and corresponding SAED patterns for b) cycled $SDRHA_{60}$ and c) C—HC before and after cycling.

surface. In terms of SDRHA, further electrolyte reduction, decomposition, and Li^+ consumption occur during the cycling processes leading to thickening of SEI. This agrees with the previous findings that SDRHA electrodes were covered with thicker SEIs due to their higher SSAs and porosities.

The O 1s XPS core-level spectra of cycled $SDRHA_{60}$ electrodes show a primary peak at ≈533.3 eV attributed to O—Si—O—Si bonds. Another dominant peak at ≈531.8 eV is attributed to overlap of Li_xSiO_y, (Li)—C—O, and P—O bonds.[59] The weaker peak at ≈533.4 eV is assigned to Si—O, C—O, and C═O bonds. In contrast, the C—HC electrode shows a more intense peak at 534.6 eV originating from Li_2CO_3, consistent with the above C 1s results.[60] Li_2CO_3 seems to be absent from SDRHA cycled anodes suggesting this Li consumption mechanism is not operative.

The main peak fitted in Si 2p spectra for cycled $SDRHA_{60}$ electrodes peak is ascribed to Si—O—Si bonding at 102.3 eV, while a small peak at ≈104.6 eV is probably associated with Si—O—C bonds, where Si in both instances is in the 4^+ valence state. This is consistent with the above observation on intimate carbon-SiO_2 interfaces. Meanwhile, the appearance of an additional peak at lower binding energies of ≈101 eV indicates lower valence states. This observation agrees with the deoxidization/partial lithiation of some SiO anodes reported in the literature,[57,59,61] likely due to the formation of silicates.[28] Typical Si^0 (≈99 eV) and Li_xSi (≈96 eV) peaks at lower energy ranges are not observed in the Si 2p spectra for cycled $SDRHA_{60}$ indicating SiO_2 reduction to Si metal is not observed at any point.

The SAED diffraction patterns show faint peaks and amorphous rings appearing in both cycled $SDRHA_{60}$ (Figure 7b) and C—HC (Figure 7c), in contrast to clear amorphous rings in pristine samples (Figures 2d and 7c), indicate partial crystallinity after cycling. This indicates that the lithiation/delithiation processes alter HC structures, possibly by dilating turbostratic nanodomains.[62] Some Li^+ was retained in inner areas in the porous structures, irreversible capacities were revealed in the electrochemical performance, consistent with the low CEs and capacity losses in C—HC. However, given the high SSAs of SDRHA, this trapped Li^+ is slowly recovered during extended cycling, resulting in the incremental increases in capacity seen in Figure 4e.

3. Conclusions

Herein, we reported a more thorough assessment of SDRHA produced by depolymerizing SiO_2 as discussed previously.[4,5,3,6–8,19,63] HC structures consisting of mixtures of amorphous and graphitized carbon domains are found in SDRHA carbon components by a combination of Raman spectroscopy, MAS NMR, and STEM. The HC in SDRHA is highly porous with significant numbers of C—O bonds due to intrinsic mixing with SiO_2.

The EDLC contributions increase with HC to SiO_2 ratios, i.e., $SDRHA_{60}$ to $SDRHA_{40}$, suggesting higher SSAs and pore volumes facilitate ion adsorption/desorption processes and consequently improve their rate capabilities. The high SSAs of SDRHA also led to low initial CEs of ≈50% and thicker SEIs. At low rate, as demonstrated by the Dunn method, diffusion-controlled processes dominate charge storage. Galvanostatic cycling of SDRHA exhibits more than two-fold higher capacities compared to C—HC. On extended cycling at C/10, capacity increments are observed. Given the isolated SiO_2 from SDRHA was demonstrated to deliver only a very small portion of total SDRHA capacities, these observations indicate that the capacity increments are related to partial lithiation of SiO_2 combined with slowly Li^+ diffusion in porous HC during extended cycling. In addition, postmortem studies on the cycled SDRHA showed evidence of $LiSi_xO_y$. SAED diffraction patterns suggest that SDRHA changes from amorphous before cycling to semi-crystalline after

cycling, which further supports the Li^+ diffusion into inner pores and intercalation between graphitic areas.

These lithiation processes might still be a factor that retard the wider implementing of RHA-derived materials for Li^+ systems, it is expected that this article provides useful insights for further scouting biomass precursors for alkali-ion storage application.

4. Experimental Section

Synthesis and Characterization of Silica-Depleted Rice Hull Ash (SDRHA) and Half-Cell Assembly: The detailed extraction of SiO_2 from RHA (Wadham Energy Inc.) to recover SDRHA and distill spirosiloxane was reported elsewhere.[20,19,6] The main steps include first milling in dilute hydrochloric acid (HCl) and repeatedly boiling in DI water to remove impurities, followed by reacting with hexylene glycol (HG) and KOH catalyst at 200 °C. To control the dissolved SiO_2 content, e.g., to produce $SDRHA_{40}$ rather than $SDRHA_{60}$, reaction times and HG volumes introduced to the reaction were adjusted. When heating is terminated and no more HG is added, the SiO_2:C ratios are fixed in the recovered SDRHA. The hard carbon was removed by oxidizing at 600 °C for 2 h/O_2.

Material Characterization: X-ray diffraction (XRD) was acquired by Rigaku Miniflex diffractometer with Cu-Kα radiation ($k = 0.154$ nm). Raman spectra were collected using a Bruker Bravo spectrometer with a 532 nm excitement laser. BET specific surface area (SSA) analyses were conducted using a Micromeritics ASAP 2020 sorption analyzer. Samples were degassed at 300 °C/6 h prior to analyses by N_2 physisorption at -196 °C (77 K). BET method using 10 data multipoint with relative pressures of 0.05–1 was applied. The pore volume was calculated based on the Barret–Joyner–Halenda (BJH) model. A JEOL JSM-IT300HR Scanning electron microscopy (SEM) was used to acquire the microstructure images and EDX maps of SDRHA. The thermogravimetric analysis (TGA) was run on a Q600 simultaneous TGA/DSC equipment. Samples were tested at 800 °C with a ramp rate of 10 °C min^{-1} in the presence of O_2 (60 mL min^{-1}). ^{13}C and ^{29}Si magic-angle spinning (MAS) nuclear magnetic resonance (NMR) spectroscopy was performed with a Bruker Avance 500 MHz spectrometer at a magnetic field of 11.7 T, corresponding to resonance frequencies of 125.8 and 99.4 MHz, respectively. Spinning was performed in 2.5 mm rotors at 20 kHz. Spectra were acquired with a $\pi/2$ pulse duration of 4.5 µs for ^{13}C and 3.3 µs for ^{29}Si, and a recycle delay of 8 s for ^{13}C and 30 s for ^{29}Si. X-ray photoelectron spectroscopy (XPS) was measured on a Kratos Axis Ultra system at room temperature under 3.1×10^{-8} Pa using monochromatic Al source (14 kV and 8 mA). The binding energies of all the elements were calibrated relative to C 1s at 284.8 eV, analyzed using CasaXPS software. Peak fitting settings 80% Gaussian and 20% Lorentzian shape with 1–1.7 eV FWHM. Raman spectra were obtained in a Renishaw inVia, wavelength 532 nm. Scanning transmission electron microscopy (STEM) images, selected area electron diffraction (SAED) patterns, and simultaneously acquired (high-angle annular dark-field) HAADF and (electron energy-loss spectroscopy) EELS maps were performed on a Talos F200X G2 (Thermo Fisher) operated at 200 keV. HAADF and EELS maps were collected with a probe current of 115 pA, a probe semi-angle of 10.5 mrad, inner collection semi-angle of about 31.5 mrad and a dwell time of 55 ms at each pixel.

Electrochemical Performance Evaluation: The SDRHA electrodes were prepared with 80 wt% SDRHA or SiO_2, 5 wt% C_{65}, and 15 wt% poly(vinylidene fluoride) (PVDF) binder. The commercial hard carbon (C—HC, MSE Supplies Inc.) and commercial graphite (C-G, Superior Graphite) electrodes were prepared with the same ratios. All powders were dried at 80 °C/vacuum overnight and dry-mixed by mortar and pestle, which was then mixed with PVDF binder solution (5 wt% solution in NMP) using a speed mixer. The uniform slurries were then coated onto a copper foil (16 µm thick) using a 150 µm gap die at a controlled speed of 50 mm s^{-1}. After drying at 80 °C/vacuum/2 h, it was punched into 18 mm electrodes. Half-cells were assembled with the SDRHA and commercial material electrodes, with Li metal used as the counter electrode in the format of 2023 coin cells. The metallic Li (16 mm) was scraped to remove the oxide layer and expose a clean surface before cell assembly. Celgard 2400 (19 mm) was used as a separator and 1.2 M $LiPF_6$ in EC:DMC (3:7 weight ratio) as the electrolyte. Data shown in the article was averaged of three cells. The assembly of full cells with NMC_{622} cathodes was reported in the previous studies.[6]

A Bio-Logic SP-300 was used to measure the AC impedance and cyclic voltammetry (CV). The EIS data was recorded in a frequency range of 7 MHz to 1 Hz with an AC amplitude of 10 mV. The CV tests were conducted in the range of 0.01–3 V with a scan rate of 0.1, 0.5, 1, 3, 5, 7, 10 mV s^{-1}. Specific capacitances are calculated per $C_{specific} = (\int Idv)/(\Delta V \times m \times r)$, where I is the current density, V is the potential range (2.99 V), r is the corresponding scan rate, and m is the mass of SDRHA. The galvanostatic cycling of the half-cells was performed between 0.01 and 2.5 V versus Li/Li^+ using a multi-channel Bio-Logic test system. For dQ/dV analyses, the data were down sampled to reduce noise. The peak positions were observed repeatedly, thus that they should reveal electrochemical redox events.

The half-cells after completing 150 cycles at C/10 were decrimped in the glovebox after delithiation and relaxation at 2.5 V. The collected electrodes were soaked and rinsed with diethyl carbonate (DEC) solvent to remove residual $LiPF_6$ salt that are not inherent to the SEI. The electrodes were then dried under vacuum at room temperature overnight before further characterization. The coatings on the cycled electrodes were scraped from the current collector using a razor blade for characterization.

Supporting Information

Supporting Information is available from the Wiley Online Library or from the author.

Acknowledgements

The authors acknowledge a generous gift from Mercedes-Benz Research & Development North America (MBRDNA) supporting this work. The authors thank Wadham Energy Inc., Williams, CA for supplying the rice hull ash used in this research. The authors thank Professor Yiyang Li's group for providing commercial hard carbon materials and providing insights and support. The authors acknowledge the Michigan Center for Materials Characterization for use of the instruments and staff assistance. The authors also thank contributions from undergraduate students Clara Huang and Daniel Casey at the University of Michigan.

Conflict of Interest

The authors declare no conflict of interest.

Author Contributions

M.Y. prepared all the samples, conducted material characterization, performed all electrochemical measurements and associated data analysis, and wrote the manuscript. M.W. assisted with SDRHA syntheses. S. I. collected the MAS NMR spectra and provided insights. J.M. and A.S. helped collect and interpret the STEM data under Robert Hovden's supervision. R.M.L. supervised the research and assisted with writing the manuscript.

Data Availability Statement

The data that support the findings of this study are available in the supplementary material of this article.

Keywords

biowaste, electrochemical characterization, hard carbon, lithium ion

Received: September 3, 2024
Revised: October 30, 2024
Published online:

[1] Z. Shi, S. Wang, Y. Jin, L. Zhao, S. Chen, H. Yang, Y. Cui, R. Svanberg, C. Tang, J. Jiang, W. Yang, P. G. Jönsson, T. Han, *SusMat* **2023**, *3*, 402.
[2] D. Surovtseva, E. Crossin, R. Pell, L. Stamford, *J. Ind. Ecol.* **2022**, *26*, 964.
[3] J. C. Marchal, D. J. K. Iii, P. McDonnell, K. Sun, R. M. Laine, *Green Chem.* **2015**, *17*, 3931.
[4] M. Yu, E. Temeche, S. Indris, R. M. Laine, *Green Chem.* **2021**, *23*, 7751.
[5] C.-D. Li, M.-U. Saeed, N. Pan, Z.-F. Chen, T.-Z. Xu, *Mater. Des.* **2016**, *107*, 440.
[6] E. Temeche, M. Yu, R. M. Laine, *Green Chem.* **2020**, *22*, 4656.
[7] M. Yu, E. Temeche, S. Indris, W. Lai, R. M. Laine, *Green Chem.* **2022**, *24*, 4061.
[8] M. Yu, E. Temeche, S. Indris, R. M. Laine, *J. Electrochem. Soc.* **2023**, *170*, 070504.
[9] Q. Xu, T. Ji, S.-J. Gao, Z. Yang, N. Wu, *Materials* **2018**, *12*, 39.
[10] K. Chen, V. Goel, M. J. Namkoong, M. Wied, S. Müller, V. Wood, J. Sakamoto, K. Thornton, N. P. Dasgupta, *Adv. Energy Mater.* **2021**, *11*, 2003336.
[11] Y. Jin, Z. Shi, T. Han, H. Yang, H. D. Asfaw, R. Gond, R. Younesi, P. G. Jönsson, W. Yang, *Processes* **2023**, *11*, 764.
[12] H. Fujimoto, K. Tokumitsu, A. Mabuchi, N. Chinnasamy, T. Kasuh, *J. Power Sources* **2010**, *195*, 7452.
[13] S. C. Chelgani, M. Rudolph, R. Kratzsch, D. Sandmann, J. Gutzmer, *Miner. Process. Extr. Metall. Rev.* **2016**, *37*, 58.
[14] C. Mao, M. Wood, L. David, S. J. An, Y. Sheng, Z. Du, H. M. Meyer, R. E. Ruther, D. L. Wood, *J. Electrochem. Soc.* **2018**, *165*, A1837.
[15] A. D. Jara, A. Betemariam, G. Woldetinsae, J. Y. Kim, *Int. J. Min. Sci. Technol.* **2019**, *29*, 671.
[16] S. Wijitkosum, P. Jiwnok, *Appl. Sci.* **2019**, *9*, 3980.
[17] A. Tomczyk, Z. Sokołowska, P. Boguta, *Rev. Environ. Sci. Biotechnol.* **2020**, *19*, 191.
[18] M. Gale, T. Nguyen, M. Moreno, K. L. Gilliard-AbdulAziz, *ACS Omega* **2021**, *6*, 10224.
[19] X. Zhang, E. Temeche, R. M. Laine, *Green Chem.* **2020**, *22*, 7491.
[20] R. M. Laine, J. C. Furgal, P. Doan, D. Pan, V. Popova, X. Zhang, *Angew. Chem.* **2016**, *128*, 1077.
[21] A. C. Ferrari, *Solid State Commun.* **2007**, *143*, 47.
[22] A. Merlen, J. G. Buijnsters, C. Pardanaud, *Coatings* **2017**, *7*, 153.
[23] P. Puech, M. Kandara, G. Paredes, L. Moulin, E. Weiss-Hortala, A. Kundu, N. Ratel-Ramond, J.-M. Plewa, R. Pellenq, M. Monthioux, *C* **2019**, *5*, 69.
[24] A. Ramar, M. Sakthivel, F.-M. Wang, K.-C. Ho, *Carbon* **2023**, *213*, 118223.
[25] M. V. Mokeev, A. V. Gribanov, Y.u. N. Sazanov, *Russ. J. Appl. Chem.* **2011**, *84*, 111.
[26] R. Blume, D. Rosenthal, J.-P. Tessonnier, H. Li, A. Knop-Gericke, R. Schlögl, *ChemCatChem* **2015**, *7*, 2871.
[27] D. J. Morgan, *C* **2021**, *7*, 51.
[28] C. Powell, *NIST X-ray Photoelectron Spectroscopy Database, NIST Standard Reference Database Number 20*, National Institute of Standards and Technology, Gaithersburg MD, **2000**, https://dx.doi.org/10.18434/T4T88K.
[29] A. Fujimoto, Y. Yamada, M. Koinuma, S. Sato, *Anal. Chem.* **2016**, *88*, 6110.
[30] M. Thommes, K. Kaneko, A. V. Neimark, J. P. Olivier, F. Rodriguez-Reinoso, J. Rouquerol, K. S. W. Sing, *Pure Appl. Chem.* **2015**, *87*, 1051.
[31] I. S. Protsak, Y. M. Morozov, W. Dong, Z. Le, D. Zhang, I. M. Henderson, *Nanoscale Res. Lett.* **2019**, *14*, 160.
[32] S. Qu, W. Wu, Y. Wu, Y. Zhuang, J. Lin, L. Wang, Q. Wei, Q. Xie, D.-L. Peng, *Nanomaterials* **2021**, *11*, 3393.
[33] J. Wang, J. Polleux, J. Lim, B. Dunn, *J. Phys. Chem. C* **2007**, *111*, 14925.
[34] Y. Jiang, J. Liu, *Energy Environ. Mater.* **2019**, *2*, 30.
[35] K. J. Aoki, J. Chen, Y. Liu, B. Jia, *J. Electroanal. Chem.* **2020**, *856*, 113609.
[36] A. Shellikeri, V. Watson, D. Adams, E. E. Kalu, J. A. Read, T. R. Jow, J. S. Zheng, J. P. Zheng, *J. Electrochem. Soc.* **2017**, *164*, A3914.
[37] C. Chen, Y. Huang, Y. Zhu, Z. Zhang, Z. Guang, Z. Meng, P. Liu, *ACS Sustainable Chem. Eng.* **2020**, *8*, 1497.
[38] H. Moon, M. Zarrabeitia, E. Frank, O. Böse, M. Enterría, D. Saurel, I. Hasa, S. Passerini, *Batteries Supercaps* **2021**, *4*, 960.
[39] B. Campbell, R. Ionescu, Z. Favors, C. S. Ozkan, M. Ozkan, *Sci. Rep.* **2015**, *5*, 14575.
[40] L. Qie, W.-M. Chen, Z.-H. Wang, Q.-G. Shao, X. Li, L.-X. Yuan, X.-L. Hu, W.-X. Zhang, Y.-H. Huang, *Adv. Mater.* **2012**, *24*, 2047.
[41] G. Zhou, D.-W. Wang, F. Li, L. Zhang, N. Li, Z.-S. Wu, L. Wen, G. Q. (Max) Lu, H.-M. Cheng, *Chem. Mater.* **2010**, *22*, 5306.
[42] S. Laruelle, S. Grugeon, P. Poizot, M. Dollé, L. Dupont, J.-M. Tarascon, *J. Electrochem. Soc.* **2002**, *149*, A627.
[43] S. Grugeon, S. Laruelle, L. Dupont, J.-M. Tarascon, *Solid State Sci.* **2003**, *5*, 895.
[44] T. Placke, O. Fromm, S. F. Lux, P. Bieker, S. Rothermel, H.-W. Meyer, S. Passerini, M. Winter, *J. Electrochem. Soc.* **2012**, *159*, A1755.
[45] M. Khan, X. Ding, H. Zhao, Y. Wang, N. Zhang, X. Chen, J. Xu, *J. Electron. Mater.* **2022**, *51*, 3379.
[46] G. M. Carroll, M. C. Schulze, T. R. Martin, G. F. Pach, J. E. Coyle, G. Teeter, N. R. Neale, *ACS Appl. Energy Mater.* **2020**, *3*, 10993.
[47] Q. Sun, B. Zhang, Z.-W. Fu, *Appl. Surf. Sci.* **2008**, *254*, 3774.
[48] B. Philippe, R. Dedryvère, M. Gorgoi, H. Rensmo, D. Gonbeau, K. Edström, *J. Am. Chem. Soc.* **2013**, *135*, 9829.
[49] M. Schnabel, E. Arca, Y. Ha, C. Stetson, G. Teeter, S.-D. Han, P. Stradins, *ACS Appl. Energy Mater.* **2020**, *3*, 8842.
[50] F. Sato, T. Honma, T. Komatsu, K. Shinozaki, T. Ina, H. Yamauchi, *J. Phys. Chem. Solids* **2022**, *161*, 110377.
[51] L. Wang, X. Wang, Z. Meng, H. Hou, B. Chen, *J. Mater. Sci.* **2017**, *52*, 7140.
[52] H. Chu, Q. Wu, J. Huang, *Colloids Surf., A* **2018**, *558*, 495.
[53] C. Ban, B. B. Kappes, Q. Xu, C. Engtrakul, C. V. Ciobanu, A. C. Dillon, Y. Zhao, *Appl. Phys. Lett.* **2012**, *100*, 243905.
[54] B. Guo, J. Shu, Z. Wang, H. Yang, L. Shi, Y. Liu, L. Chen, *Electrochem. Commun.* **2008**, *10*, 1876.
[55] J. Park, S. Suh, S. Tamulevičius, D. Kim, D. Choi, S. Jeong, H.-J. Kim, *Nanomaterials* **2022**, *12*, 2625.
[56] P. Viswanath, M. Yoshimura, *SN Appl. Sci.* **2019**, *1*, 1519.
[57] Z.-Y. Wu, L. Deng, J.-T. Li, S. Zanna, A. Seyeux, L. Huang, S.-G. Sun, P. Marcus, J. Światowska, *Batteries* **2022**, *8*, 271.
[58] H. Adenusi, G. A. Chass, S. Passerini, K. V. Tian, G. Chen, *Adv. Energy Mater.* **2023**, *13*, 2203307.
[59] J. Chen, X. Fan, Q. Li, H. Yang, M. R. Khoshi, Y. Xu, S. Hwang, L. Chen, X. Ji, C. Yang, H. He, C. Wang, E. Garfunkel, D. Su, O. Borodin, C. Wang, *Nat. Energy* **2020**, *5*, 386.
[60] K. N. Wood, G. Teeter, *ACS Appl. Energy Mater.* **2018**, *1*, 4493.
[61] M. Miyachi, H. Yamamoto, H. Kawai, T. Ohta, M. Shirakata, *J. Electrochem. Soc.* **2005**, *152*, A2089.
[62] J. Lu, Z. Zhang, Y. Zheng, Y. Gao, *Adv. Mater.* **2023**, *35*, 2300359.
[63] E. Temeche, X. Zhang, R. M. Laine, *ACS Appl. Polym. Mater.* **2021**, *3*, 2144.